Physics and Imaging in Radiation Oncology 32 (2024) 100644

Contents lists available at ScienceDirect

Physics and Imaging in Radiation Oncology

journal homepage: www.sciencedirect.com/journal/physics-and-imaging-in-radiation-oncology

Original Research Article

Monte Carlo-based simulation of virtual 3 and 4-dimensional cone-beam computed tomography from computed tomography images: An end-to-end framework and a deep learning-based speedup strategy

Frederic Madesta [a,b,c,*], Thilo Sentker [a,b,c], Clemens Rohling [a,b,c], Tobias Gauer [d], Rüdiger Schmitz [a,b,c], René Werner [a,b,c]

[a] Institute for Applied Medical Informatics, University Medical Center Hamburg-Eppendorf, Hamburg 20246, Germany
[b] Department of Computational Neuroscience, University Medical Center Hamburg-Eppendorf, Hamburg 20246, Germany
[c] Center for Biomedical Artificial Intelligence (bAIome), University Medical Center Hamburg-Eppendorf, Hamburg 20246, Germany
[d] Department of Radiotherapy and Radiation Oncology, University Medical Center Hamburg-Eppendorf, Hamburg 20246, Germany

ARTICLE INFO

Keywords:
Monte Carlo simulation
Cone-beam computed tomography
Computed tomography
Deep learning speedup

ABSTRACT

Background and purpose:: In radiotherapy, precise comparison of fan-beam computed tomography (CT) and cone-beam CT (CBCT) arises as a commonplace, yet intricate task. This paper proposes a publicly available end-to-end pipeline featuring an intrinsic deep-learning-based speedup technique for generating virtual 3D and 4D CBCT from CT images.

Materials and methods:: Physical properties, derived from CT intensity information, are obtained through automated whole-body segmentation of organs and tissues. Subsequently, Monte Carlo (MC) simulations generate CBCT X-ray projections for a full circular arc around the patient employing acquisition settings matched with a clinical CBCT scanner (modeled according to Varian TrueBeam specifications). In addition to 3D CBCT reconstruction, a 4D CBCT can be simulated with a fully time-resolved MC simulation by incorporating respiratory correspondence modeling. To address the computational complexity of MC simulations, a deep-learning-based speedup technique is developed and integrated that uses projection data simulated with a reduced number of photon histories to predict a projection that matches the image characteristics and signal-to-noise ratio of the reference simulation.

Results:: MC simulations with default parameter setting yield CBCT images with high agreement to ground truth data acquired by a clinical CBCT scanner. Furthermore, the proposed speedup technique achieves up to 20-fold speedup while preserving image features and resolution compared to the reference simulation.

Conclusion:: The presented MC pipeline and speedup approach provide an openly accessible end-to-end framework for researchers and clinicians to investigate limitations of image-guided radiation therapy workflows built on both (4D) CT and CBCT images.

1. Introduction

Intermodal image comparison and matching have profound implications in radiation therapy. For instance, the comparison of fan-beam computed tomography (CT) and cone-beam CT (CBCT) arises as a commonplace, yet intricate task [1]. In this paper, we endeavor to advance CBCT-to-CT matching for clinical and research tasks through a publicly available end-to-end pipeline for the generation of virtual 3D and 4D CBCT from CT images. Furthermore, we also present a learning-based speedup technique for this computationally expensive task.

During the course of treatment, the comparison of daily CBCT and planning CT images is used for patient positioning, typically through manual or semi-automated rigid registration of characteristic bone markers [2] and, depending on the specific clinical workflow, subsequent rigid soft tissue-based region of interest alignment. Especially adaptive radiation therapy workflows would benefit from a more precise local CT-to-CBCT matching, applying deformable image registration (DIR) of soft tissue structures to account for anatomical changes caused by bowel or bladder filling, patient weight fluctuations, treatment effects, and to update target volumes during therapy. However, DIR of CT

* Corresponding author.
E-mail address: f.madesta@uke.de (F. Madesta).

https://doi.org/10.1016/j.phro.2024.100644
Received 16 April 2024; Received in revised form 30 August 2024; Accepted 6 September 2024
Available online 12 September 2024

and CBCT images suffers from different image characteristics of the two imaging modalities. Furthermore, enhanced visual comparability facilitated by virtual CBCT (CBCT to CBCT comparison, i.e., intra- instead of inter-image modality comparison) allows for the early detection of anatomical or tumor changes compared to the initial CT, thereby improving the monitoring and adaptation of treatment strategies [3,4]. In particular, a virtual time-resolved CBCT simulated from a corresponding planning 4D CT would allow for the assessment of the reference tumor motion but represented by a CBCT.

Moreover, virtual CBCT images can pave new ways for various research endeavors: Firstly, with virtual CBCT images computed from any archived CT image, the presented approach will enhance the availability of CBCT images for machine learning studies, e.g., tumor detection or organ segmentation, especially when combined with real-world clinical data. Specifically, CT-based annotations can directly be used on corresponding virtual CBCT images. A second field of application could be the boosting of the image quality of low-quality sparse-view 4D CBCT images. While the application of machine learning methods has already shown promising potential [5], the development of such models is limited by the scarcity of low- and high-quality 4D CBCT images of an identical anatomical setting. With our method, this data can directly be generated from the same underlying fan-beam CT image, thus, ensuring that the virtual CBCT images closely resemble the clinical data encountered in practice. Thirdly, since there is currently no broadly accepted standard setting for 4D CBCT acquisitions (compare, e.g., [6] to [7]), optimizing scanning parameters remains an open task. Our method allows the simulation of CBCT images with arbitrary scanning parameters from CT ground truth images, that is, no (or only a small amount) CBCT images have to be acquired for scanning parameter optimization.

Despite its potential impact, widespread adoption of virtual CBCT image generation is currently hampered by computational costs and the multitude of necessary sub-steps. These steps encompass the segmentation of the original CT, mapping the segmented regions to chemical compositions and physical properties, and the computationally expensive Monte Carlo (MC) simulation of individual projections [8]. To tackle practical and computational complexity, this work aims at the following contributions:

(1) Introduction of an end-to-end simulation framework for generating (virtual) CBCT from CT images.
(2) Proposition of a deep learning (DL)-based acceleration method for the MC simulation.
(3) Demonstration of the application of our framework and evaluation of the acceleration method using both phantom and routine clinical data.
(4) Extension of the simulation process to include time-resolved, i.e., 4D CBCT scans through the use of correspondence models to correlate internal patient motion information and external respiratory signal.

The framework is available at github.com/IPMI-ICNS-UKE/4d-cbct-mc.

2. Materials and methods

2.1. Extraction of physical properties from CT intensity information

First, a 3D-U-Net to segment upper body organs (lung, liver, stomach), and additionally bones, muscles, fat, lung vessels, and tissue/other (i.e., all remaining volumes) was trained. Please refer to the supplemental materials for details. Secondly,we extracted the elemental compositions for the segmented organs and tissues from the Adult Reference Computational Phantoms report [9]. This involved assigning the most suitable matching material to each mask. We divided bones into intensity-dependent submasks to precisely differentiate between less and more dense bone structures, ensuring accurate material assignments. High-Z materials, like gold markers near the tumor, are mapped to the respective chemical material by thresholding the CT image with a high Hounsfield value. The patient geometry is then fully specified by the obtained material and density images $I_{\mathrm{mat}}, I_{\rho}$.

The elemental compositions of the materials are employed to calculate the cross-sections for photon interactions with the material according to

$$\sigma_{\mathrm{comp}}(E) = \sum_{i=1}^{N_{\mathrm{el}}} w_i \sigma_i(E), \tag{1}$$

where w_i is the mass fraction weight factor of the i-th element in the material composition consisting of N_{el} elements and $\sigma_i(E)$ is the total cross-section of the i-th element at energy E. Furthermore, the total cross-sections are categorized into partial cross-sections for Rayleigh scattering, Compton scattering, photoelectric absorption, and pair production, respectively, based on the XCOM database [10].

2.2. Monte Carlo simulations

MC simulations utilized an extended version of a GPU-based MC backend [11]. We accurately matched the MC geometries and parameters to the applied clinical CBCT imager of the Varian TrueBeam, integrating the specifications provided by the manufacturer. Each MC simulation produced a stack of $i = 1, \ldots, n_{\mathrm{proj}}$ normalized projections $P_{i,\mathrm{norm}}$. A detailed description is given in the supplemental materials.

Image reconstruction. The normalized projections P_{norm} obtained were corrected for beam hardening effects (cf. Section 2.3) and subsequently reconstructed utilizing the open source Reconstruction Toolkit (RTK), which features highly efficient GPU-based 3D and 4D CBCT reconstruction algorithms. By default, the Feldkamp, Davis, and Kress (FDK, [12]) algorithm was used for 3D image reconstruction. For clinically and virtually acquired projection data, identical FDK parameter sets are employed.

2.3. Calibration/evaluation phantoms and strategies

Calibration. To determine the number of photons n_{hist}, i.e., the number of photon histories tracked during simulation, required to match the image noise level of the Varian TrueBeam CBCT imager, a real-world reference scan of the CatPhan604 calibration phantom (The Phantom Laboratory Inc., Salem, NY, USA, cf. Fig. 2 b) was acquired. The CatPhan604 is a cylindrical phantom featuring various inserts for assessing image quality and geometric/physical accuracy. A corresponding simulation phantom was generated and used for MC simulations.

Both the measured and simulated CatPhan604 scans were reconstructed and compared with respect to the image noise level σ_{noise}. The number of photon histories n_{hist} was adjusted until the noise level of the simulated scan matched the measured noise level (see Fig. 2 a). The optimization process was considerably accelerated by taking advantage of the fact that the additive white Gaussian image noise is proportional to the inverse square root of the number of photon histories. Thus, the following fit function was applied after generating a few $(n_{\mathrm{hist}}, \sigma_{\mathrm{noise}})$ samples:

$$\sigma_{\mathrm{noise}}(n_{\mathrm{hist}}) = A\frac{1}{\sqrt{n_{\mathrm{hist}}}}, \quad \text{with fit parameter } A \in \mathbb{R}^{+}. \tag{2}$$

The resulting number of photon histories was then used for all subsequent reference MC simulations. To account for beam hardening effects, water precorrection, following the methodology introduced by Sourbelle et al. [13], was implemented using a simulated and a real scan of the CatPhan604.

Evaluation. The evaluation of the performed simulations employed

different strategies. Physically measurable metrics and the CatPhan604 phantom were used to quantify the general simulation performance. This included comparing attenuation coefficients in various material inserts (see Fig. 2b) of the CatPhan604 phantom for both the scanned and simulated CBCT images. Furthermore, the proposed image-impression-conserving DL-based speedup model, which aims to prevent increased image noise levels due to a reduced number of simulated photons (see Fig. 2a), was evaluated using the peak signal-to-noise ratio (PSNR). The image resolution was quantified by simulating a line pair phantom with and without speedups and analyzing it using the corresponding modulation transfer functions (MTF). Additionally, a qualitative analysis of the performance was conducted using the CIRS Dynamic Thorax phantom (CIRS, Norfolk, VA, USA), focusing on the end-to-end workflow for a fully time-resolved simulation. Patient data was used to evaluate the performance for real clinical data (cf. Section 2.4 for CT data description).

2.4. DL-based MC speedup

To reduce the long computation times of MC simulations with a substantial number of photon histories, a DL-based MC speedup approach was developed. In the following, CBCT projections and corresponding reconstructed images are denoted as P and R, with additional information given in superscript (real: measurement; MC: simulation; MC, ☆: simulation with DL-based speedup) and subscript (ref: reference, $1/x$: factor by which n_{hist} is reduced in the simulation).

As illustrated in Fig. 1 b, an encoder-decoder model, here, a 2D U-Net [14], was trained to map a MC projection $P^{\text{MC}}_{1/x}$ simulated with a x-times lower number of photon histories to a projection $P^{\text{MC}}_{\text{ref}}$ simulated with the reference number of photon histories (cf. Table 1). To guide the network, additional geometrical information is provided in the form of a forward projection P_{fwd} of the density image I_ρ, which is computed by summing up the density values along the X-ray paths for each projection angle.

The employed training data consists of in–house acquired, artifact-free 3D CT image data (image spatial resolution: 0.98 mm × 0.98 mm × 2 mm, image dimensions in voxels: 512 × 512 × [150–160]; data acquisition with Siemens Definition AS Open, Siemens Healthineers, Germany) from 21 patients split into train ($n = 15$) and test set ($n = 6$). For each CT data set, CBCTs (894 projections per CBCT) were MC simulated for five different speedup settings, i.e., 1/50, 1/40, 1/30, 1/20 and 1/10 of the default number of photon histories were used. In total,

Table 1
Default MC parameters for simulation of virtual CBCT scans. Parameter selection was based on the specific CBCT scan acquisition protocol and the installed treatment machine. Simulation speed is given for an average patient geometry.

Name	Value
scan mode	half-fan (160 mm lateral detector displacement)
tube voltage	125 kVp
foil filter	0.89 mm Ti
n_{hist} per projection for $P^{\text{MC}}_{\text{ref}}$	$1.37{\cdot}10^{10}$
n_{proj}	894
angular coverage	2π
source to isocenter	1000 mm
source to detector	1500 mm
detector size	$1024 \times 768\,\text{px}^2$
detector pixel size	$0.388 \times 0.388\,\text{mm}^2$
simulation speed	$2.35{\cdot}10^8$ hist/s (per GPU)

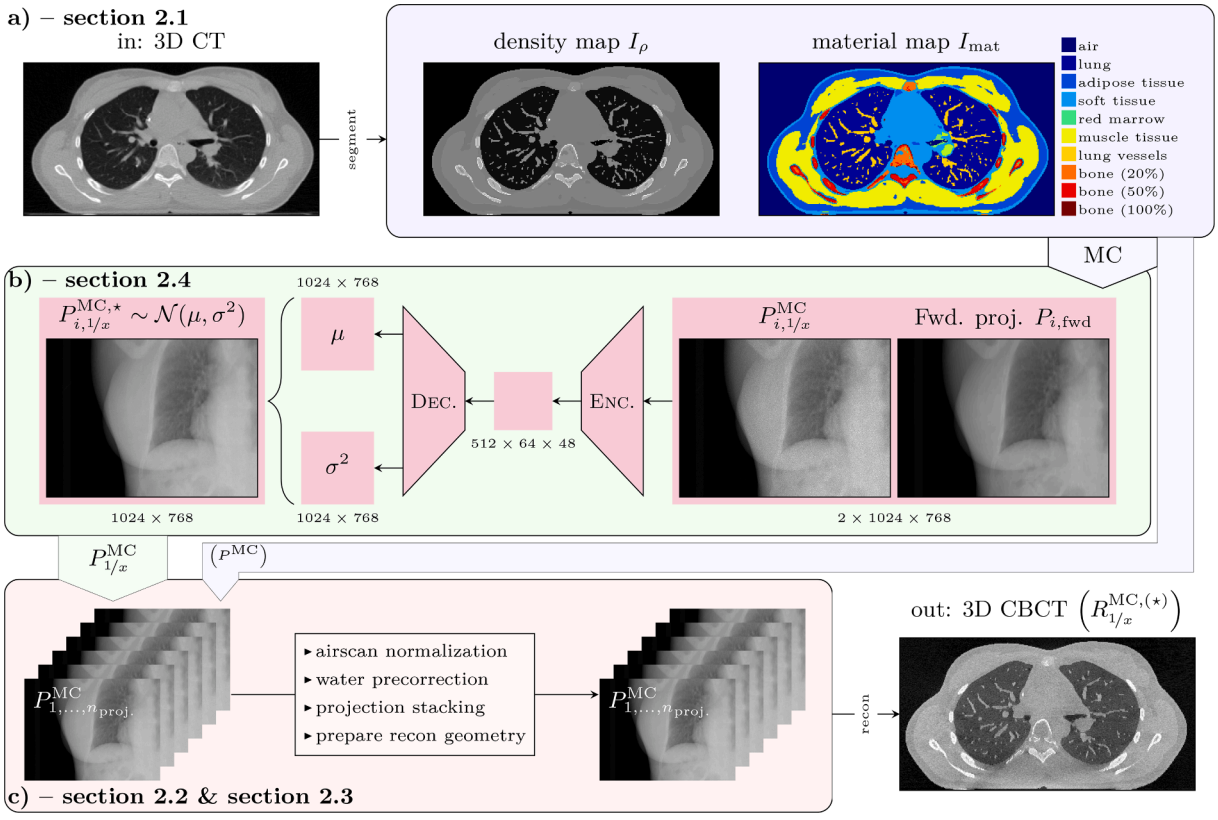

Fig. 1. Proposed workflow for MC simulation of a 3D CBCT scan from CT data. Block a) The initial 3D CT data undergoes automatic segmentation, yielding the density and material maps required for MC simulation. Block b) The output of the MC simulation, along with the forward projection, is fed into the proposed MC speedup network. This network generates a μ and σ^2 map, facilitating the sampling of projection data that mirrors characteristics (e.g., PSNR) of simulated data obtained from more extensive simulations. Note that this speedup block is optional. Block c) The sampled data is normalized and corrected before all projections are used for reconstruction, resulting in the sought 3D CBCT image.

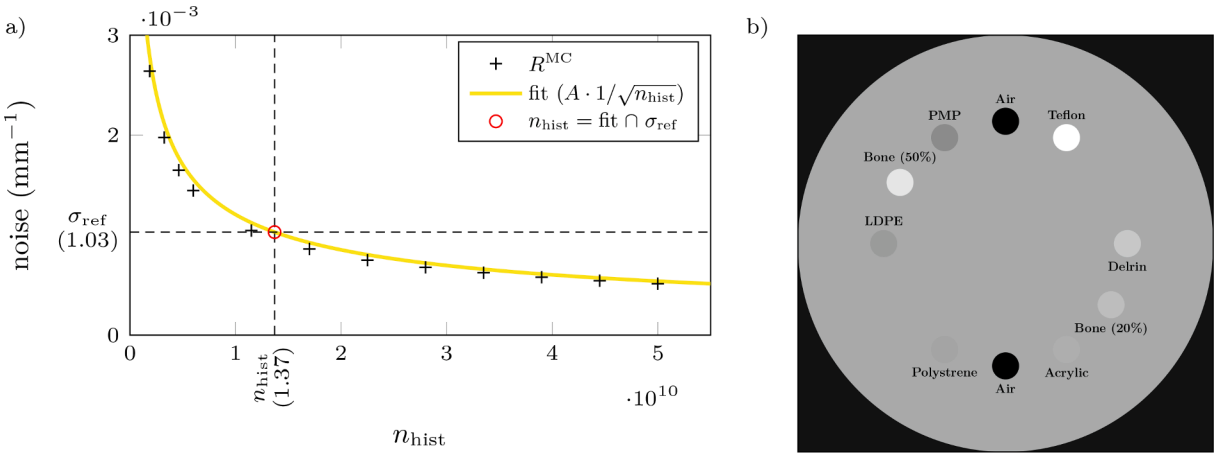

Fig. 2. a) Estimation of n_{hist} by fitting simulated to measured noise. b) Schematic illustration of an axial slice of the CatPhan604 phantom with inserts.

$5 \times 15 \times 894 = 67,050$ train and $5 \times 6 \times 894 = 26,820$ test projections were available. The retrospective data evaluation was approved by the local ethics board, and the need to obtain written informed consent was waived [WF-82/18].

However, training such a model with common loss functions incorporating L_p-norms will not yield realistic output projections $P^{\text{MC},\star}_{1/x}$ as the network will just return a smoothed version of the input projection $P^{\text{MC}}_{1/x}$. Since the MC simulations were performed with a high number of photons, the Poisson noise of the $P^{\text{MC}}_{\text{ref}}$ projections can be approximated by a Gaussian distribution $\mathcal{N}(\mu, \sigma^2)$ with mean μ and variance σ^2. Consequently, the network can be trained to predict (μ, σ^2) for each detector pixel by minimizing the Gaussian negative log-likelihood loss function

$$\mathscr{L}(\mu, \sigma^2) = \frac{1}{2}\left(\log\left(\max(\sigma^2, \epsilon)\right) + \frac{\left(\mu - P^{\text{MC}}_{\text{ref}}\right)^2}{\max(\sigma^2, \epsilon)}\right), \quad \epsilon \in \mathbb{R}^+, \tag{3}$$

where ϵ is a small constant to avoid numerical instabilities. The final projections $P^{\text{MC},\star}_{1/x}$ were then sampled from the predicted Gaussian distributions, resulting in projections with the same noise characteristics as the reference projections $P^{\text{MC}}_{\text{ref}}$. As the computation time required by the MC simulation is proportional to the number of photon histories and the proposed speedup model is computationally fast (~ 60 ms per projection), the overall speedup factor is given by x.

2.5. Simulation of time-resolved CBCT scans

The patient's anatomy undergoes changes during scanning due to respiratory motion. While this typically has no impact on the 3D CT image impression as the acquisition time ($\sim$1 s) is smaller than the average breathing period ($\sim$5 s), the effect becomes noticeable for 3D CBCT scans with scan times of $\sim$60 s, where the resulting image is in consequence blurred. To achieve a realistic CBCT image impression with the proposed MC simulations framework, it becomes necessary to consider such motion. Thus, the static patient phantom geometry as described in Section 2.2 has to be warped for each individual X-ray projection to realistically simulate a CBCT for a patient, regardless of whether the image should be reconstructed in 3D or 4D. In doing so, the now time-resolved MC simulation has a time resolution equal to the number of projections per second (here 15 s^{-1}, cf. Table 1). A common approach for deformably transforming the patient anatomy based on a low-dimensional breathing signal involves using correspondence models. In this study, internal motion data from 4D CT scans is correlated with external breathing signals of the same patient to predict internal motion states when a new breathing pattern is introduced [15]. For detailed information, please refer to supplemental materials (Suppl. C). The fitted correspondence model was used to deform the patient phantom—both its density and material image—for each projection angle according to the external patient breathing signal acquired during CBCT imaging at that specific time point.

3. Results

First, the default MC simulation setting was evaluated using the simulation parameters as defined in Table 1. A visual comparison between $R^{\text{MC}}_{\text{ref}}$ and $R^{\text{real}}_{\text{ref}}$ CBCT images of the CatPhan604 phantom demonstrated a close alignment of edges, indicating an accurate simulation of the scan geometry. Additionally, the obtained attenuation coefficients in various material inserts are compared in Fig. 3a and show good agreement with a mean deviation of 1.7%.

Secondly, an analysis of the proposed DL-based MC speedup model on resulting CBCT images is performed. The application of the proposed speedup model significantly improves the projection noise level and yields good accordance with the reference noise level in $P^{\text{MC}}_{\text{ref}}$ as evaluated by the PSNR in Fig. 3c. The depicted MTF in Fig. 3b, illustrates that the spatial resolution of the reconstructed image $R^{\text{MC},\star}_{1/x}$ perfectly matches the reference image $R^{\text{MC}}_{\text{ref}}$, even for the highest speedup factor of $x = 50$. Consequently, the proposed DL-based speedup model does not introduce any additional blurring to the reconstructed image.

In Fig. 4, the end-to-end workflow is evaluated by comparing $R^{\text{MC}}_{\text{ref}}$, $R^{\text{MC},\star}_{1/50}$, $R^{\text{MC}}_{1/50}$ and respective $R^{\text{real}}_{\text{ref}}$ scans for the CIRS phantom. Especially the CBCT-typical streaking artifacts that occur in the image domain after reconstruction over all acquired projections (i.e., obtaining a temporal average image) are similar between $R^{\text{MC}}_{\text{ref}}, R^{\text{MC},\star}_{1/50}$ and real CBCT data. Furthermore, image characteristics (noise, edges, blurring, etc.) are almost identical.

In Fig. 5, a patient data-based evaluation of the proposed pipeline is shown. Here, a full end-to-end test is conducted, particularly employing the correspondence model fitted using the planning 4D CT data, which is subsequently applied using the respiratory curve of the real CBCT scan to predict the time-resolved internal deformation. The influence of the respiratory motion on the CBCT image impression, i.e., the presence of streaking artifacts and an increased noise/blurring level, is visible when compared to the static patient simulation in Fig. 1c right (see supplemental materials for a detailed side-by-side comparison). Comparing $R^{\text{MC},\star}_{1/20}$ to $R^{\text{MC}}_{\text{ref}}$ depicts the effect of the proposed DL-based speedup model (20-fold speedup based on findings in Fig. 3c), where even the smallest structures match. A comparison of the vector fields obtained by DIR in 4D CT and 4D CBCT of the same patient and the same motion patterns is

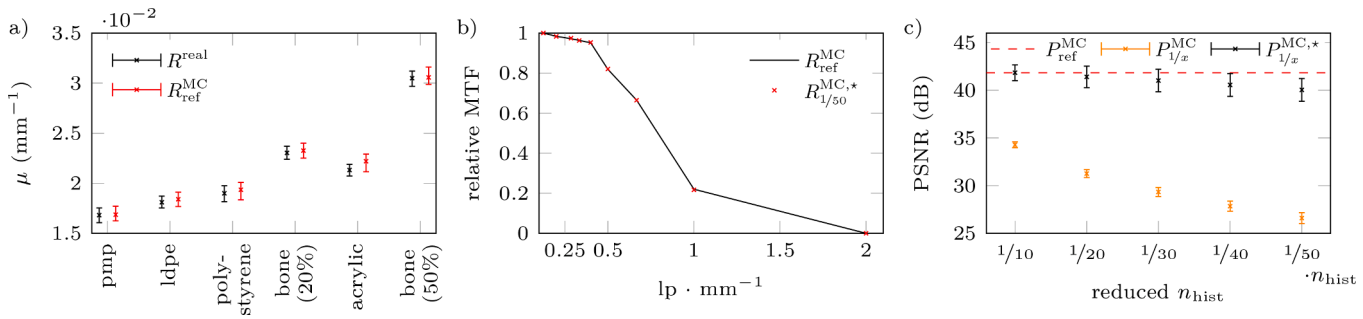

Fig. 3. a) Comparison of attenuation coefficients μ for various material inserts of the CatPhan604 phantom extracted from reference measurement and default MC simulation. b) Image resolution evaluated by a line pair (lp) test for MC simulations with and without DL-based speedup. c) Projection PSNR as a function of MC simulations with reduced number of photon histories with and without DL-based speedup compared to the reference simulations of the test subset.

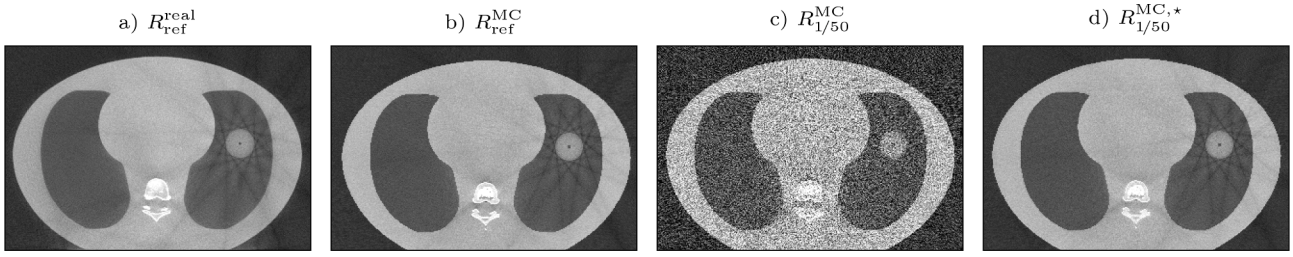

Fig. 4. Average CBCT images of the CIRS phantom reconstructed from measured and simulated time-resolved projection data acquired while the tumor insert was in motion ($\cos^4$-motion with 5.0 s period and $\pm$10 mm amplitude). From left to right: a) Measured reference, b) simulated reference, c) simulated with 1/50 photon histories and d) simulated with 1/50 photon histories and DL-based speedup. Note that the streaks are solely caused by the motion of the tumor insert and would not be present in a static scan. In c), streaks are not visible due to the increased image noise.

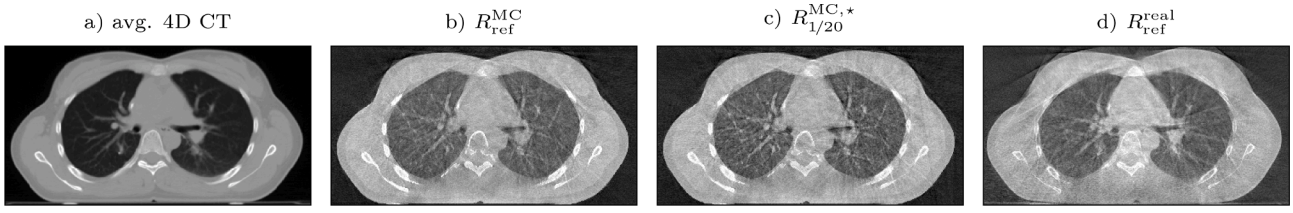

Fig. 5. End-to-end test of the proposed pipeline. Based on the planning 10-phase 4D CT data, with the corresponding temporal average image shown in subfigure a), a correspondence model is fitted using the 4D CT respiratory signal. The breathing curve acquired during scanning of the real CBCT (subfigure d) is used for correspondence model inference to simulate a fully time-resolved 4D CBCT scan with and without DL-based speedup, cf. time-averaged reconstructions in sub-figure c) and b), respectively. A detailed comparison can be found in the supplemental materials.

presented in the supplemental materials (fig. F.3).

Quantitatively, the mean absolute differences (in units of mm^{-1}) of the CIRS phantom simulations to the real scan were 0.0024, 0.0011 and 0.0011 ($R^{\text{MC}}_{1/50}, R^{\text{MC},\star}_{1/50}, R^{\text{MC}}_{\text{ref}}$). The patient study had slightly larger errors with 0.0037, 0.0027, 0.0027 ($R^{\text{MC}}_{1/20}, R^{\text{MC},\star}_{1/20}, R^{\text{MC}}_{\text{ref}}$). To put these numbers into context, the homogeneous tissue-equivalent material of the real CIRS scan was evaluated and showed a noise-related standard deviation of 0.0011 mm^{-1}.

4. Discussion

In this study, a fully integrated pipeline for generation of virtual 3D and 4D CBCT images from initial 3D CT images is presented. It employs MC simulations as a backbone to ensure high geometric and physical accuracy and robustness (to, e.g., out-of-distribution patient/phantom geometries). To mitigate the high computational times associated with MC simulations, a DL-based speedup strategy is introduced. The acceleration is achieved by simulating a reduced number of photon histories, and the resulting projections are subsequently modified by a deep neural network. Leveraging additional information from the CT image, the neural network aims to obtain projections as if they were simulated from a substantially larger number of photon histories (up to 50 times for simpler geometries like imaging phantoms and up to 20 times for patient data). This combined approach significantly speeds up computation while preserving important image characteristics.

From a methodological point of view, our approach is a hybrid one, between purely MC-based simulation [16] and purely deep learning. Latter approaches are typically GAN-based methods [17]. Whilst GANs overcome the extreme computational demand of full MC simulations, they suffer from limited and, importantly, poorly guaranteed physical accuracy and unclear adaption to unseen scenarios. Our method merges advantages of both approaches: Being based on MC-simulated X-ray projections and standard reconstruction, physical accuracy in unseen scenarios is ensured, and the speedup is achieved through use of a DL model only for a well-defined sub-task. The balance between exact MC simulation and DL-based speedup can be flexibly adjusted. This combination ensures not only accuracy but also flexibility in handling a wide range of scenarios, making the pipeline adaptable to diverse applications in CBCT imaging. In this context and to highlight the generalizability, it is noteworthy that the proposed model performs well on CIRS phantom data, even though it is trained exclusively on patient data.

To the best of our knowledge, a fully automatic end-to-end 4D CBCT MC-based simulation framework has not been proposed in the literature so far. Similar methods, e.g. [18,19], employ MC for simulating CBCT projections but lack automatic tissue segmentation and realistic 4D respiratory modelling. For the first time, the proposed framework allows to investigate whether DIR in 4D CT and 4D CBCT of the same patient that represent the same motion patterns lead to the same motion vector fields. As shown in the supplemental materials, this is not the case, demonstrating that further research is necessary in that direction.

Despite the strengths of the proposed approach, it also comes with certain limitations that warrant careful consideration. The assumption of an ideal detector may lead to discrepancies between simulated and real-world imaging conditions. Moreover, the reliance on average population-based chemical compositions for organs, potentially overlooking individual variations in composition that may affect the accuracy of the simulations. Theoretically, this could be mitigated by introduction of an additional correction step based on the CT-measured Hounsfield units. However, on the whole, these limitations only marginally impact simulation accuracy, especially for 4D CBCT. When dealing with different scan protocols, the speedup model may require retraining to ensure optimal performance. This is especially relevant for different X-ray spectra or tube settings. However, full retraining is not necessary, as the model can be efficiently fine-tuned starting with an existing model. Changes of the entire scan geometry or geometry-related parameters like lateral detector displacement, number of projections, or the projection frame rate do not require any additional actions as this information is always included in the forward projection P_{fwd} fed into the model.

Funding Statement

This work was funded by DFG research grants WE 6197/2–1 and WE 6197/2–2 (project number 390567362). RW and TG were supported by a research grant from Siemens Healthineers AG. We acknowledge financial support from the Open Access Publication Fund of University Medical Center Hamburg-Eppendorf.

Declaration of Competing Interest

The authors declare that they have no known competing financial interests or personal relationships that could have appeared to influence the work reported in this paper.

Acknowledgements

We thank J. Wasserthal for providing additional TotalSegmentator [20] models weights for fat, muscle, and tissue segmentation under academic license.

Appendix A. Supplementary material

Supplementary data associated with this article can be found, in the online version, at https://doi.org/10.1016/j.phro.2024.100644.

References

[1] Molitoris JK, Diwanji T, Snider III JW, Mossahebi S, Samanta S, Onyeuku N, et al. Optimizing immobilization, margins, and imaging for lung stereotactic body radiation therapy. Transl Lung Cancer Res 2019;8:24–31. https://dx.doi.org/10.21037/tlcr.2018.09.25.
[2] Schwarz M, Cattaneo GM, Marrazzo L. Geometrical and dosimetrical uncertainties in hypofractionated radiotherapy of the lung: a review. Phys Med 2017;36:126–39. https://doi.org/10.1016/j.ejmp.2017.02.011.
[3] Bellec J, Arab-Ceschia F, Castelli J, Lafond C, Chajon E. ITV versus mid-ventilation for treatment planning in lung SBRT: a comparison of target coverage and PTV adequacy by using in-treatment 4D cone beam CT. Radiat Oncol 2020;15. doi: 10.1186/s13014-020-01496-5.
[4] den Otter LA, Anakotta RM, Weessies M, Roos CTG, Sijtsema NM, Muijs CT, et al. Investigation of inter-fraction target motion variations in the context of pencil beam scanned proton therapy in non-small cell lung cancer patients. Med Phys 2020;47:3835–44. https://doi.org/10.1002/mp.14345.
[5] Madesta F, Sentker T, Gauer T, Werner R. Self-contained deep learning-based boosting of 4D cone-beam CT reconstruction. Med Phys 2020;47:5619–31. https://doi.org/10.1002/mp.14441.
[6] Hansen DC, Sørensen TS. Fast 4D cone-beam CT from 60s acquisitions. Phys Imaging Radiat Oncol 2018;5:69–75. https://doi.org/10.1016/j.phro.2018.02.004.
[7] Balik S, Weiss E, Jan N, Roman N, Sleeman WC, Fatyga M, et al. Evaluation of 4-dimensional Computed Tomography to 4-dimensional Cone-Beam Computed Tomography Deformable Image Registration for Lung Cancer Adaptive Radiation Therapy. Int J Radiat Oncol Biol Phys 2013;86:372–9. https://doi.org/10.1016/j.ijrobp.2012.12.023.
[8] Badal A, Badano A. Fast Simulation of Radiographic Images Using a Monte Carlo X-Ray Transport Algorithm Implemented in CUDA, Elsevier, 813–829. 2011. doi: 10.1016/b978-0-12-384988-5.00050-4.
[9] ICRP. Adult Reference Computational Phantoms. ICRP Publication 110. Ann ICRP, 2009, 39.
[10] Berger M. XCOM: photon cross sections database. NIST, 2010. https://dx.doi.org/10.18434/T48G6X.
[11] Badal A, Badano A. Accelerating Monte Carlo simulations of photon transport in a voxelized geometry using a massively parallel graphics processing unit. Med Phys 2009;36:4878–80. https://doi.org/10.1118/1.3231824.
[12] Feldkamp LA, Davis LC, Kress JW. Practical cone-beam algorithm. J Opt Soc Am A 1984;1:612. https://doi.org/10.1364/josaa.1.000612.
[13] Sourbelle K, Kachelrieb M, Kalender W. Empirical water precorrection for cone-beam computed tomography. In IEEE Nuclear Science Symposium Conference Record. 2005;4:1871–5. https://doi.org/10.1109/NSSMIC.2005.1596696.
[14] Ronneberger O, Fischer P, Brox T. U-Net: Convolutional Networks for Biomedical Image Segmentation. In Navab N, Hornegger J, Wells WM, Frangi AF, editors, Medical Image Computing and Computer-Assisted Intervention – MICCAI 2015. Cham: Springer International Publishing, 2015, 234–41. doi: 10.1007/978-3-319-24574-4_28.
[15] Wilms M, Werner R, Ehrhardt J, Schmidt-Richberg A, Schlemmer H, Handels H. Multivariate regression approaches for surrogate-based diffeomorphic estimation of respiratory motion in radiation therapy. Phys Med Biol 2014;59:1147–64. https://doi.org/10.1088/0031-9155/59/5/1147.
[16] Abbani N, Baudier T, Rit S, Franco Fd, Okoli F, Jaouen V, et al. Deep learning-based segmentation in prostate radiation therapy using Monte Carlo simulated cone-beam computed tomography. Med Phys 2022;49:6930–44. https://dx.doi.org/doi.org/10.1002/mp.15946.
[17] Dahiya N, Alam SR, Zhang P, Zhang SY, Li T, Yezzi A, et al. Multitask 3D CBCT-to-CT translation and organs-at-risk segmentation using physics-based data augmentation. Med Phys 2021;48:5130–41. https://dx.doi.org/doi.org/10.1002/mp.15083.
[18] Shieh C, Gonzalez Y, Li B, Jia X, Rit S, Mory C, et al. SPARE: Sparse-view reconstruction challenge for 4D cone-beam CT from a 1-min scan. Med Phys 2019;46:3799–811. https://doi.org/10.1002/mp.13687.
[19] Jia X, Gu X, Graves YJ, Folkerts M, Jiang SB. GPU-based fast Monte Carlo simulation for radiotherapy dose calculation. Phys Med Biol 2011;56:7017–31. https://doi.org/10.1088/0031-9155/56/22/002.
[20] Wasserthal J, Breit HC, Meyer MT, Pradella M, Hinck D, Sauter AW, et al. TotalSegmentator: robust segmentation of 104 anatomic structures in CT Images. Radiol Artif Intell 2023;5. doi: 10.1148/ryai.230024.